

A parametric study of the concentric-ring transducer design for MRI guided ultrasound surgery

Todd Fjield, Xiaobing Fan, and Kullervo Hynynen

Department of Radiology, Brigham and Women's Hospital, Harvard Medical School, LMRC G-007,
221 Longwood Avenue, Boston, Massachusetts 02115

(Received 13 September 1995; accepted for publication 24 March 1996)

Noninvasive surgery using high-powered, focused ultrasound transducers in conjunction with magnetic resonance imaging has been shown to be feasible in previous studies. For clinical treatments, the geometry of standard MRI equipment limits the space available for ultrasound surgical equipment. This space requirement can be reduced in one dimension by using phased arrays to control the focal depth, thus eliminating the space required for the motion of a fixed focus transducer. Because of its symmetry, an annular array is ideal for changing the focal depth. Previous works have simulated, built, and characterized various concentric-ring transducers; however, no study has thoroughly examined the potential and limitations of the concentric-ring design for MRI guided ultrasound surgery. The present work is a systematic examination of the capabilities of the concentric-ring array, using numerical simulations to predict the power field, temperature distribution, and accumulated thermal dose. The results presented here illustrate the effects of ring size, center-to-center spacing configurations, number of rings, and radius of curvature on transducer performance. A 10-cm radius of curvature transducer with 14 evenly spaced rings has been built and characterized in order to verify the accuracy of the numerical simulations. The pressure-squared fields produced by this transducer are in excellent agreement with the simulated fields. © 1996 Acoustical Society of America.

PACS numbers: 43.80.Vj, 43.80.Sh [FD]

INTRODUCTION

High-powered, focused ultrasound beams were first used to create lesions deep in tissue by Lynn *et al.*, in 1942. Since then, various studies have demonstrated the feasibility of using ultrasound for several therapies (Fry *et al.*, 1955; Lele, 1962; Kishi *et al.*, 1975; Fry and Johnson, 1978; Heimburger, 1985; Coleman *et al.*, 1985; Vallencian *et al.*, 1992; Bihrlé *et al.*, 1994). However, because the transmission of ultrasound can be affected by tissue geometry, real time feedback is necessary to insure safe, controlled treatment (Fan and Hynynen, 1992; Fan and Hynynen, 1994).

Previous studies have shown that it is possible to detect temperature elevations in tissue via magnetic resonance imaging (Parker, 1984; De Poorter, 1995). MRI can provide real-time feedback on the thermal effects with enough spatial and thermal accuracy to be utilized in guiding ultrasound surgery (Hynynen *et al.*, 1993; Darkazanli *et al.*, 1993; Cline *et al.*, 1992). The current configuration for focused ultrasound surgery consists of a fixed-focus, spherically curved ultrasound transducer mounted on a three-axis positioning system (Cline *et al.*, 1995; Hynynen *et al.*, 1996). The patient and the surgical apparatus are positioned within the bore of the MR magnet. MR data are used to reference the current position of the focus, determine the boundaries of the tissue to be treated, and monitor the temperature elevation of the tissue. Due to the nature of the standard MRI equipment, space is limited, and thus it is important to minimize the volume occupied by the surgical equipment. While sufficient motion along the surface of the patient can be accomplished in a relatively small space by using mechanical positioning

systems, the small openings of the clinical magnets limit mechanical motion in the depth direction.

One way to reduce the space requirement in the depth direction is to utilize electrical focusing. The concentric-ring design is ideal for electrically moving a focus in one dimension due to its axial symmetry. This type of array has been used for ultrasonic imaging of deep tissues (Arditi *et al.*, 1981), and in 1981, Do-Huu and Hartemann (1981) explored the possibility of using an annular array transducer for deep hyperthermia. Their results showed that the concentric-ring design was feasible (Do-Huu and Hartemann, 1982), however their array's operating frequency was 400 kHz, which is not ideal for tissue ablation (Hynynen, 1991). Others have also simulated the heating patterns of various concentric-ring designs for hyperthermia (Cain and Umemura, 1986; Ibbini and Cain, 1990), and some investigators have explored the use of the concentric-ring array for ablation, including Chapelon *et al.* (1993), who constructed two small, 6-ring transducers for the treatment for benign prostatic hyperplasia (BPH) and prostate cancer. In 1994, a 10-ring array designed for deep tissue ablation was built and characterized (Zanelli *et al.*, 1994), however, the ring configuration and the fact that they only removed the electrode between the rings as opposed to cutting completely through the ceramic limited the transducer's performance. Although arrays of this type have been simulated and built, a comprehensive study of the concentric-ring design specifically for use in MRI guided ultrasound surgery has yet to be performed.

The present work systematically examines the theoretical capabilities of various concentric-ring transducer configurations for ultrasound surgery via numerical simulations.

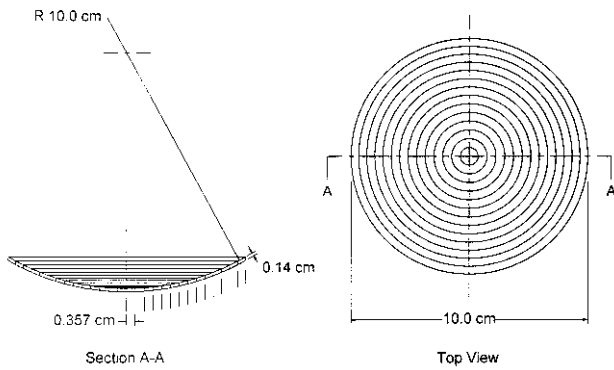


FIG. 1. Schematic illustrating the concentric-ring design.

Transducer parameters such as number of rings, relative center-to-center ring spacing, and geometric focus were varied and simulated. In addition, construction constraints were estimated and accounted for, in an attempt to design a transducer with a maximum focal range that is also practical to build. To support the theoretical results, a 14-ring transducer has been constructed and tested, and its actual performance has been compared to that as simulated.

I. MATERIALS AND METHODS

A. Spherically curved concentric-ring geometry

The geometry of the simulated concentric-ring transducers consists of a spherically curved ultrasonic radiator divided into a series of concentric-rings centered on the y axis (in MRI coordinates when the transducer is mounted on the scanner table) as shown in Fig. 1. The width of each ring was measured in the XZ plane, and the rings were numbered from the center outward in ascending order, with the center element designated as the first ring (the center element can be considered a ring with an outside diameter equal to the diameter of the disk and the inside diameter of 0 mm). The maximum total diameter of the transducer was limited to 10 cm. The transducer frequency chosen is 1.5 MHz, as an earlier study has shown this to be a good compromise between the cavitation threshold and the attenuation of the ultrasound in tissue (Hynynen, 1991).

An air-backed ultrasonic transducer was modeled, and hence the acoustic power was assumed to radiate only from the concave side of the radiator. The amplitude and phase of each ring were independently controlled, and there was assumed to be no dead space between adjacent elements. For all of the simulations performed, the amplitude of each ring was set such that the acoustic power output per unit area for all of the rings was equivalent.

The ring spacing configurations resulting from four different methods used to generate the ring widths were considered. The first method resulted in rings of the same width when measured on the surface of the transducer (i.e., the arc widths of the rings were equivalent.) For the second method, the transducer was projected onto the XZ plane, and the divisions were equally spaced in this plane. The requirement for the third method was similar to the method used by Zanelli *et al.* (1994): for a single, chosen point on the y axis,

the phase difference of the acoustic waves from each ring arriving at this point could vary by no more than 90° , and hence the distance from this point to the nearest and the farthest edges of each ring could vary by no more than $\lambda/4$. A point was chosen such that the total number of rings resulting from this method was equal to the number desired. The fourth method was to divide the rings in such a manner that the surface areas of all of the rings were equivalent, however, a comparison between the ring spacing resulting from the equal area method and the $\lambda/4$ deviation method shows negligible difference. Although these two methods are based on different premises, the resulting ring spacings are the same. Thus, only the first three methods of division need be separately considered.

B. Calculation of concentric-ring element phasing

The phasing for each ring was calculated from the middle of the ring, i.e., $r_n = (r_{ni} + r_{no})/2$, where r_{ni} is the inside diameter of the n th ring and r_{no} is the outside diameter, such that the phase variation from a single ring corresponds to approximately half of the simple sources leading the desired phase for the ring, and half lagging, at the focal spot. The relative phase of the n th ring was calculated as follows:

$$\theta_n = \frac{d_n - d_1}{\lambda} \cdot 360^\circ, \quad (1)$$

where d_n is the distance from the middle of the n th ring to the focus, d_1 is the distance from the first ring to the focal point, and λ is the wavelength of sound in tissue. At the frequency of 1.5 MHz, $\lambda = 1.0$ mm. (Note that the center element is designated as the first ring with an inner diameter of zero.)

C. Acoustic field calculations

To calculate the resulting pressure field of an ultrasonic transducer, the surface of the transducer is viewed as an assemblage of point sources with each source contributing a radially symmetric power field. At each point in the field, the contributions of all of the point sources are added together via superposition as described by O'Neil (1949). For a nonattenuating medium, this is accomplished by using the Rayleigh–Sommerfeld integral:

$$p_m = \frac{i\rho ck}{2\pi} \sum_{n=1}^N u_n \int_{S_n} \frac{e^{-ikr_{mnq}}}{r_{mnq}} dS_n, \quad (2)$$

where p_m is the acoustic pressure at point (x_m, y_m, z_m) , $i \equiv \sqrt{-1}$, ρ is the density of the medium, c is the speed of sound, k is the real wave number, $u_n \equiv A_n e^{i(\omega t + \theta_n)}$ is the complex excitation of all point sources on the n th element with amplitude A_n , frequency ω , and phase θ_n as explained in a preceding section, r_{mnq} is the distance to point m from a point q on element $n(x_{nq}, y_{nq}, z_{nq})$, and S_n is the surface area of element n .

Water is used as the coupling medium between the transducer and the tissue to be treated. Water is considered a nonattenuating medium, while tissue is considered a low attenuating medium. To modify Eq. (2) to take into consider-

ation the attenuation of tissue $e^{-ikr_{mnq}}$ must be replaced with $e^{-ik_c r_{mnq}}$, where $k_c = k - i\alpha$ is the complex wave number with an amplitude coefficient of attenuation α .

Once the pressure has been calculated, the power deposition per unit volume is calculated as

$$Q(x, y, z) = \mu_{\text{abs}} \frac{|p_m(x, y, z)|^2}{Z}, \quad (3)$$

where μ_{abs} is the absorption coefficient and $Z = \rho c$ is the acoustic impedance of the medium.

As Fig. 1 illustrates, the concentric-ring system is radially symmetric about the y axis. Hence, there is no pressure gradient nor temperature gradient in the azimuth direction and cylindrical symmetry can be used. Making use of this symmetry, $p_m(r, y) = p_m(x, y, 0)$, and the computation time can be dramatically reduced.

A preliminary study of the power field versus simple source spacing and field grid spacing resulted in the decision to use a simple source spacing of no more than 0.5 mm in both directions on the transducer surface (Ocheltree and Frizzell, 1989). Due to the geometry of the geometrically focused transducer, this source spacing is sufficiently small such that any further decrease in size results in a negligible increase in the accuracy of the power field while significantly increasing computation time. The same holds true for an acoustic field grid spacing of 1.0 mm in the axial direction and 0.25 mm in the radial direction. These values allowed the fastest computation time with a high degree of accuracy. The difference between the axial and radial grid spacing is a result of the difference in the magnitude of the thermal gradients produced in the two directions.

D. Thermal modeling

In order to calculate the effect of a power field on the temperature in tissue, the thermal conductivity of the tissue and the perfusion of blood through the tissue must be taken into account. The differential equation that relates these properties to the temperature is the bioheat transfer equation (Pennes, 1948):

$$\rho_t c_t \frac{\partial T}{\partial t} = k_t \nabla^2 T - \omega_b c_b (T - T_a) + Q(r, y), \quad (4)$$

where T is the temperature at time t at the location (r, y) , ρ_t is the density of the tissue, c_t is the specific heat of the tissue, k_t is the thermal conductivity of the tissue, ω_b is the blood perfusion rate, c_b is the specific heat of the blood, T_a is the arterial blood temperature, and $Q(r, y)$ is the acoustic power deposition rate per unit volume, as defined by Eq. (3). The tissue was simulated as a homogeneous medium.

The boundary conditions consisted of a temperature of 37 °C on the radial extreme of the simulated area, 37 °C on the axial end farthest from the transducer, and 25 °C and 37 °C was used at the water/tissue interface. The initial condition was 37 °C within the simulated cylinder. Preliminary investigation of the water/tissue interface boundary condition showed that using a boundary condition of 25 °C resulted in

TABLE I. Parameters used in thermal simulations.

Parameter	Value	Units
ρ_t —tissue density	998	kg/m ³
α —attenuation coefficient	5	Np/m/MHz
c_b —specific heat of blood	3770	J/kg/°C
c_t —specific heat of tissue	3770	J/kg/°C
k_t —tissue thermal conductivity	0.5	W/m/°C
ω_b —blood perfusion rate	1	kg/m ³ /s
T_a —arterial blood temperature	37	°C

a temperature difference of less than 0.1 °C along the central axis except in the first 0.5 mm from the water/tissue interface.

Previous studies have shown that there are several parameters that influence the temperature elevation in tissue (Damianou and Hynynen, 1994). For long sonication times, such as those encountered in hyperthermia, blood perfusion rate is one important parameter governing temperature elevation. However, the shorter the time of sonication, the less influence the rate of perfusion has on the temperature elevation (Billard, 1990). On the other hand, the shorter the time of sonication, the less effect conduction has on the temperature field distributions, and thus the smaller the volume of necrosed tissue. In this study sonication times of 10 s were used, as this is a good compromise between minimizing the temperature dependence on perfusion while maximizing the volume of the necrosis (Damianou and Hynynen, 1994).

Each simulation assumed there were two media layers. The surface of the tissue was 3 cm from the base of the transducer, with water between the tissue and the transducer. The speed of sound was assumed to be 1500 m/s and the density was 998 kg/m³ for both water and tissue. Table I is a comprehensive list of the parameters used in the thermal simulations. The attenuation coefficient $\alpha = 5$ Np/m/MHz was added to k_c in Eq. (2) as described above to simulate the effect of attenuation in the tissue.

A numerical finite difference approach was used to solve Eq. (4). The maximum value of the time step size which still yields accurate solutions to this equation has been shown to be dependent on the grid spacing. For the spacings quoted above, it was necessary to reduce the time step to 20 ms. The maximum temperature reached in each simulation was 100 °C at the location of the intended focus, accomplished by scaling the total acoustic output power accordingly.

E. Dose calculations

The thermal dose was calculated based on a technique suggested by Sapareto and Dewey (1984). Tissue necrosis can be predicted by calculating via a numerical integration the number of equivalent minutes at some reference temperature:

$$\text{Dose}_{T_{\text{ref}}}(t) = \int_{t=0}^{\text{final}} R^{T_{\text{ref}} - T(t)} dt \approx \sum_{t=0}^{\text{final}} R^{T_{\text{ref}} - T_{\Delta t}} \Delta t, \quad (5)$$

where T_{ref} is the reference temperature, $t_{\text{final}} = t_{\text{heating}} + t_{\text{cooling}}$, Δt is the small time interval described above, $T_{\Delta t}$ is the

average temperature over time Δt , and R is the parameter defined as

$$R = \begin{cases} 0.5, & \text{for } T(t) \geq 43^\circ\text{C}, \\ 0.25, & \text{for } T(t) < 43^\circ\text{C}. \end{cases}$$

The necrosed volume is approximated by finding the surface which encloses a volume that contains only tissue which has accumulated a thermal dose equivalent to 240 min at the reference temperature of $T_{\text{ref}} = 43^\circ\text{C}$. It has been shown that the trends of tissue necrosis induced by focused ultrasound can be estimated using this method (Damianou and Hynynen, 1994).

F. Array construction

The constructed concentric-ring array was machined from a 1.38-mm-thick, 10-cm-diam, spherically curved lead zirconate titanate (PZT-4) piezoelectric shell with a 10-cm radius of curvature. The ring configuration consisted of 14 rings equally spaced in the XZ plane, resulting in a center-to-center spacing of 3.57 mm. These rings were divided by cutting completely through the ceramic between the rings. The machining process produced a gap of approximately 0.3 mm between adjacent rings, resulting in a ring width of about 3.3 mm. The space between the elements was filled with silicone rubber in order to minimize any mechanical coupling between the rings. The ceramic was then mounted in a waterproof polycarbonate casing, allowing the transducer to be submerged while remaining air backed.

Each element of the array was connected to an LC matching circuit in order to match the array to $50\ \Omega$ at the operating frequency of the transducer. The array was driven at 1.54 MHz, and the phase of each channel was independently controlled by an in-house manufactured digital circuit with 4 bits of phase control resolution (Buchanan and Hynynen, 1994).

G. Acoustic field measurements

The 14-ring phased array was placed in a tank of degassed water. Stepper motors scanned a thermistor embedded in a small bead of silicone across the focal region of the transducer (Martin and Law, 1983). Measurements were taken every 1.0 mm in the axial direction and 0.25 mm in the radial direction. The uncertainty in the absolute location of the field is estimated to be about 1 mm in the axial direction resulting from an imprecision in the location of the starting point, and the relative accuracy of the equipment is quoted as $5\ \mu\text{m}/25\ \text{mm}$ by the scanner frame manufacturer (Daedal, Harrison City, PA). The thermistor was manually positioned only once, and therefore the 1 mm uncertainty applies only to the absolute location of the fields and not to the relative locations in and between the scans.

H. Total acoustic power measurements

The total acoustic power output from each ring was measured in degassed water via a radiation force technique (Stewart, 1982). The measurements were taken at 1.54 MHz, with the input voltages set such that the acoustic output power from each ring corresponded to a power per unit area

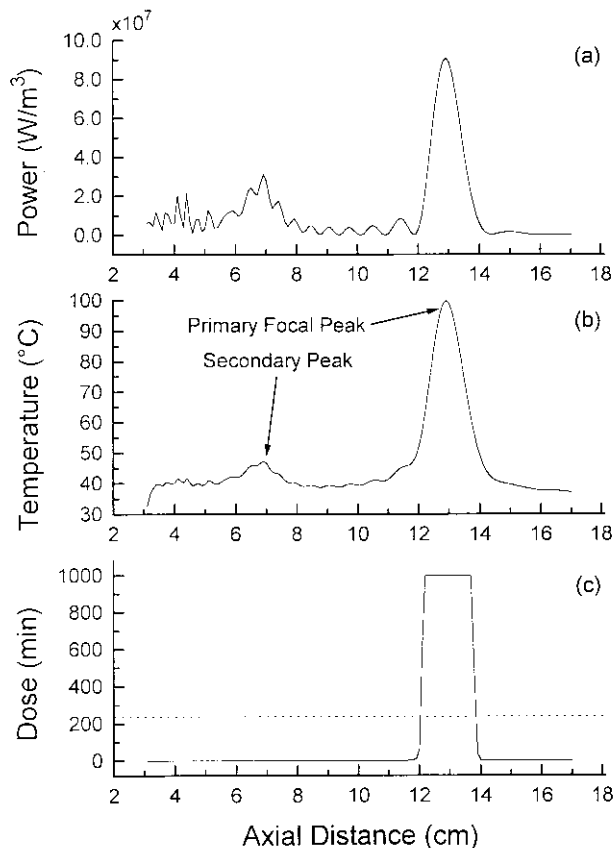


FIG. 2. Simulated results showing an example of the axial distributions of power, temperature, and thermal dose. The transducer geometry simulated consisted of 16 rings. F number 1.0 (10-cm radius of curvature) and was focused at 13 cm. (a) Axial profile of power deposited power. (b) Temperature profile generated from the power field illustrating the primary and secondary focal peaks used to characterize the transducer's performance. (c) Accumulated thermal dose received by the tissue along the transducer's center line.

of three times that required for the highest power simulated sonication in order to insure the capability of adequate power delivery for surgery. The power output from each ring was measured individually, and the results were summed to determine total transducer acoustic output power.

II. RESULTS

A. Simulation results

Figure 2 is an example of typical axial distributions of power, temperature, and thermal dose resulting from the concentric-ring array. A 16-ring, 10-cm radius of curvature transducer was the configuration used to generate this figure. The transducer is electrically focused at 13 cm, yet note the small secondary focus at approximately 7 cm. Although the location of the necrosed region is of primary interest, and no secondary region of necrosis is formed, the temperature at the secondary focus reaches at least 45°C . In the clinical environment, a temperature elevation resulting from a secondary focus may cause pain, and if not carefully monitored, an unwanted accumulation of thermal dose resulting in necrosed tissue. Considering that multiple sonications are necessary to treat an entire tumor volume, any temperature increase outside the primary focus causes an increase in

TABLE II. Comparison of the ring arc-widths for a 6-cm radius of curvature array resulting from three different methods of ring division.

Ring #	Equal radial increment	Arc width	Quarter-wavelength
1	3.57	4.22	10.50
2	3.58	4.22	6.29
3	3.61	4.22	4.88
4	3.65	4.22	4.16
5	3.71	4.22	3.71
6	3.78	4.22	3.40
7	3.87	4.22	3.16
8	3.99	4.22	2.98
9	4.14	4.22	2.83
10	4.33	4.22	2.72
11	4.58	4.22	2.62
12	4.90	4.22	2.53
13	5.35	4.22	2.46
14	6.01	4.22	2.40

treatment time, as there must be a long enough delay between sonications for the tissue at the secondary focus to cool down such that neither pain nor a second region of necrosis is formed (Damianou and Hynynen, 1993). Thus, thermal dose alone is not an adequate indicator of transducer performance. It is also difficult to estimate the temperature profile from the power profile with a sufficient degree of accuracy. Hence, the temperature profile was used as the primary indicator of transducer performance in this study.

Outside of the primary focus, a temperature elevation to 43 °C was considered the maximum acceptable secondary temperature elevation, as this is the location of the discontinuity in the equation for accumulated thermal dose, above which dose increases much more rapidly. Also, no pain is caused at this temperature. However, it is important to note that when one considers that multiple sonications are often necessary in MRI guided ultrasound surgery, more stringent requirements for secondary temperature elevation must take into account, such as the primary necrosis tissue volume, the secondary temperature elevation, and the resulting temperature increase at the secondary focus after an appropriate cool-down time between sonications (Fan and Hynynen, 1996).

The first design parameter studied was the relative center-to-center spacing of the rings. Table II lists the arc widths resulting from the three methods of division for 14 rings. The widths shown correspond to a 6-cm radius of curvature transducer, as this is the smallest radius of curvature transducer simulated, and the smaller the radius of curvature, the greater the difference between the arc width of the elements and equal-radial increment widths. Simulations were run for each of these ring configurations for transducers with various F numbers.

Figure 3 compares the results of the thermal simulations for the three ring configurations described above for 7-, 10-, and 13-cm radius of curvature transducers. A method of ring division was chosen for all subsequent simulations that would result in an array most practical for MRI guided ultrasound surgery, based on maximum focal range capability and ring widths that would be practical to realize in a constructed array. As the graphs show, the quarter-wavelength

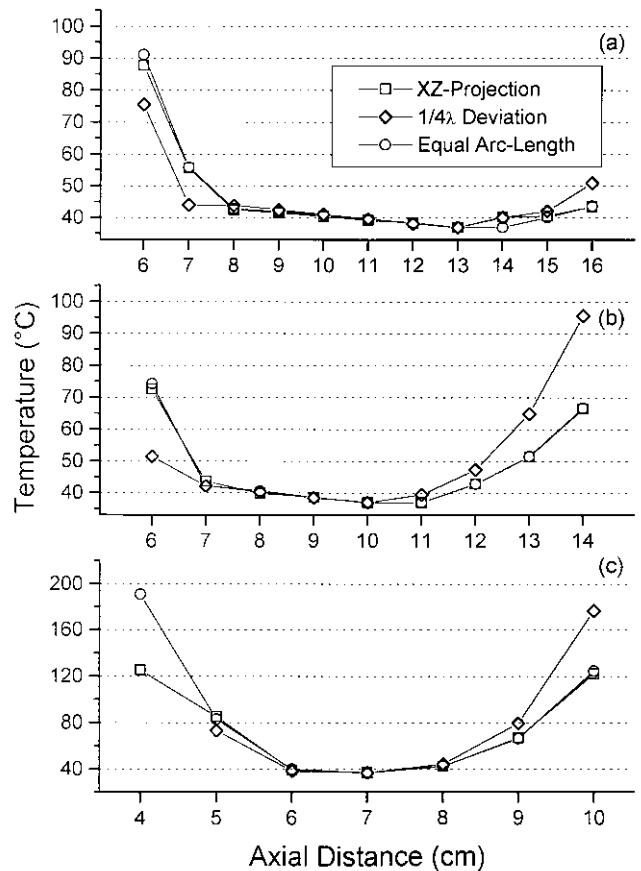


FIG. 3. Secondary temperature elevation comparison curves for three different methods of ring division. (a) F number 1.3 (13-cm radius of curvature), (b) F number 1.0 (10-cm radius of curvature), and (c) F number 0.7 (7-cm radius of curvature). Note that for each point the power was scaled such that the temperature at the primary focus was 100 °C.

deviation method produces lower secondary temperature elevations when focusing closer to the transducer than the other methods. Later, however, a method is described for reducing the secondary temperature elevations when focusing near the transducer. Utilizing this method, less emphasis needs to be placed on the secondary temperature elevations resulting when focusing near the transducer, and the focal range is more heavily dependent on the ability of the transducer to focus beyond the geometric focus. The arc-width division method and the equal-radial increment method are able to move the focus farther past the geometric focus with less secondary temperature elevation than the quarter-wavelength deviation method. However, as is shown most clearly in the case of the 7-cm radius of curvature transducer, the equal-radial increment method produces lower secondary temperature elevations at the extreme focal locations than the equal arc-width method. In addition to resulting in the largest focal range, the equal-radial increment method results in an array which is most practical to construct, in that the rings are not unacceptably small as would be the case with the equal area method if the number of rings were increased to obtain the same focal range as the equal-radial increment method. Thus, all subsequent transducer configurations simulated were based on the equal-radial increment ring division.

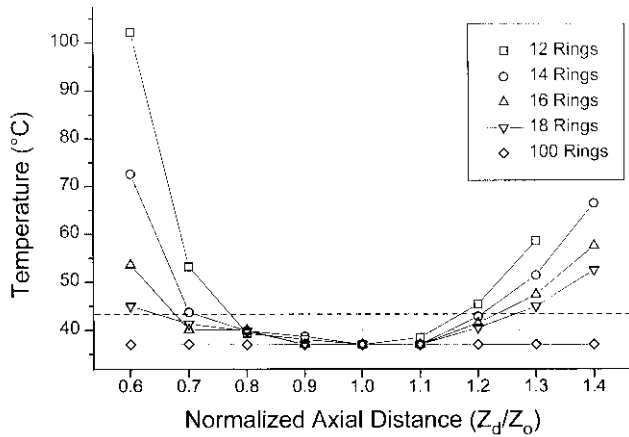


FIG. 4. Temperature comparison curves for various numbers of rings. Each curve represents the secondary temperature elevations resulting from an F number 1.0 (10-cm radius of curvature) transducer with the power scaled for each point such that the primary peak always reached 100 °C. Z_d is the distance from the face of the transducer, and Z_0 is the geometric focus of the transducer.

The next parameter considered was the number of rings. Although it is well known that the more rings a transducer has, the larger its range of focus, there are various construction limitations regarding the maximum number of rings which can be practically realized. In order to determine the

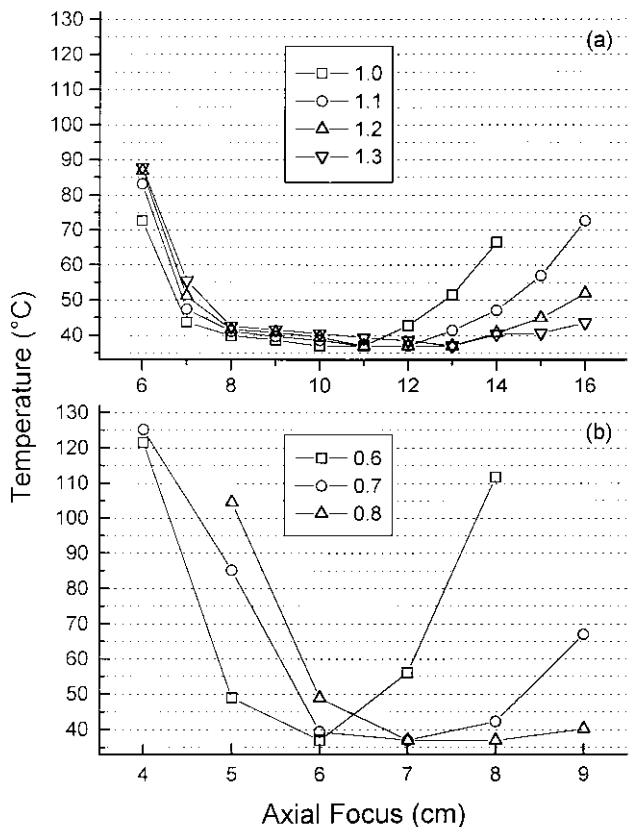


FIG. 5. Temperature comparison curves for various F numbers. Note that the diameters of the transducers remained fixed at 10 cm. Each curve represents the secondary temperature elevations resulting from a 14-ring transducer. (a) The temperature comparison curves for transducers with F numbers greater than 1.0. (b) The temperature comparison curves for transducers with F numbers less than 1.0.

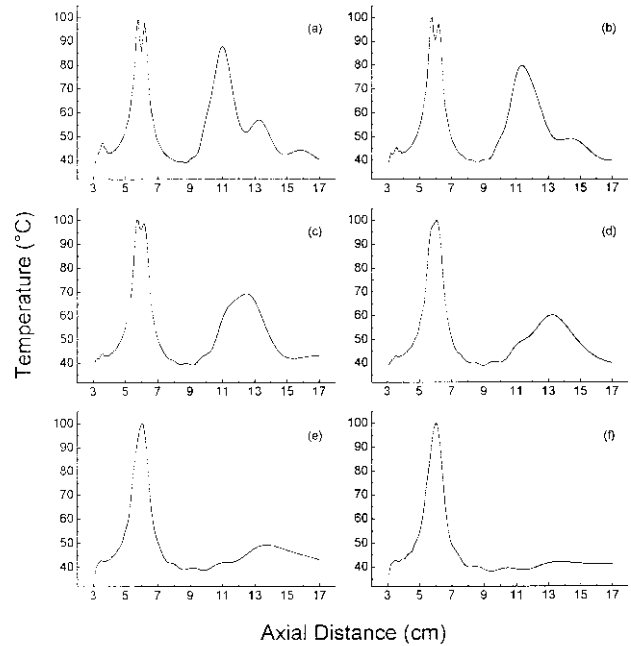


FIG. 6. Effect of turning off outer rings. These graphs represent the axial temperature distributions for a 14-ring transducer phased to focus at 6 cm with outer elements turned off. The F number of this transducer is 1.3 (13-cm radius of curvature), and the power is scaled such that the maximum temperature reached is 100 °C for each sonication. (a) The centerline profile for this transducer with all 14 rings powered. Each successive graph represents a higher effective F number achieved by powering one fewer ring, from (b) with 13 rings powered to (f) with 9 rings powered.

focal ranges achievable by transducers of practical dimension, a transducer with F number 1.0 was simulated with various numbers of rings ranging from 12 to 18 rings, resulting in ring widths from 0.417 to 0.278 cm, respectively, along with a simulation of 100 rings. Established linear array theory states that if the individual elements are less than $\lambda/2$ wide, unwanted grating lobes can be avoided at any steering angle (Steinberg, 1976; Skolnik, 1980). In the case of the geometrically focused concentric-ring array, where the steering angle from each element is generally significantly less than that of a linear array, 100 rings can be considered the ideal case.

The results of the simulations are shown in Fig. 4. These results show that the smaller the ring size, the greater the effective focal range of the transducer. While increasing the number of rings does not produce a significant increase in focal range (less than 2 cm difference between the 12-ring and the 18-ring array), increasing the number of rings significantly lowered the secondary temperature elevations resulting at the focal extremes. This property allows the increase of the focal range by further lowering the secondary temperature elevations near the face of the transducer, as will be discussed later.

For the practical array, the main limiting criteria is the minimum realizable ring width. Based on previous experience with piezoceramics, it was assumed that the minimum practical ring size is limited to about 3 mm. However, these simulations did not take into account any dead space between the rings, as this parameter is dependent on the method of construction. Many applicable construction tech-

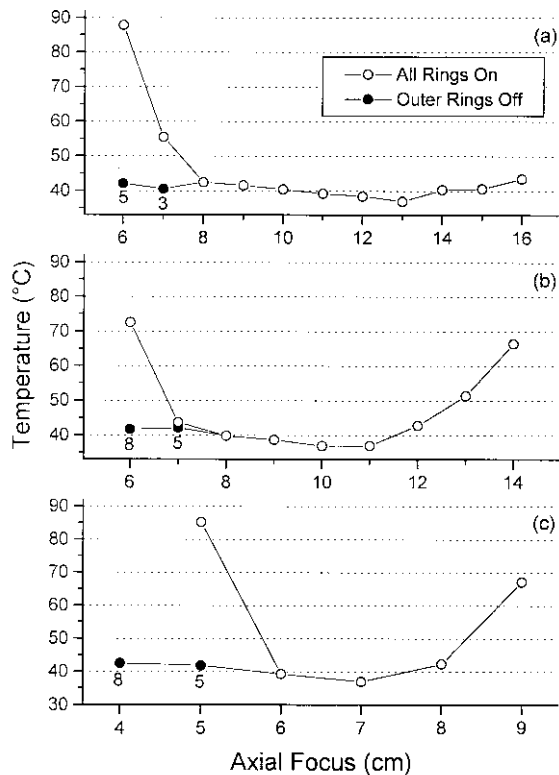


FIG. 7. Performance curves for three transducers of optimum design within preset construction limits. Each transducer has 14 rings. (a) Far focal range transducer with F number 1.3 (13-cm radius of curvature). (b) Middle focal range transducer with F number 1.0 (10-cm radius of curvature). (c) Close focal range transducer with F number 7.0 (7-cm radius of curvature). The numbers near the points represent the number of rings turned off in each case to reduce the secondary temperature elevations to below 43°C , as 43°C is considered the maximum acceptable secondary temperature elevation.

niques will yield a dead space from 0.3 to 0.5 mm, and with this in mind, 14 rings (3.57-mm center-to-center spacing) was considered as a compromise between theoretical performance and assumptions regarding construction limitations. As the goal of this study is to examine the effects of various parameters on the focal capabilities of the concentric-ring array of practical dimensions, the transducers modeled in the following simulations are all composed of 14 rings.

The effective focal range of a transducer with a given number of rings can be altered by moving the geometric focus, which translates to changing the F number of the transducer. Setting the diameter of the transducer to 10 cm and varying the F number results in the secondary temperature elevation curves shown in Fig. 5. As can be seen from the figure, the effective ranges of the transducer center around their geometric foci, and the effective range also increases with increased F number. For example, the transducer with F number 1.3 is capable of focusing over a range from 8 to 15 cm. On the other hand, the transducer with F number 1.0 was capable of focusing from 7 to 12 cm.

Division of the depth of the intended focal location by the diameter of the transducer results in an effective F number, and as shown above, a larger F number results in a larger range of focus. This would lead one to believe that in order to focus at depths near the face of the transducer, one

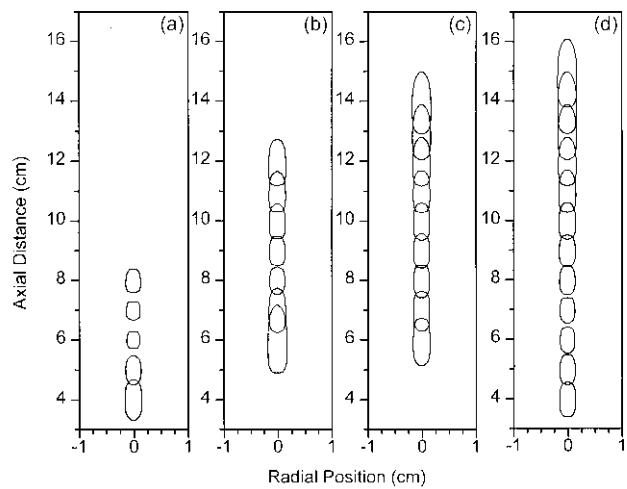


FIG. 8. Simulated necroses formed by four transducer designs with a 0.3-mm kerf between the rings: (a) 14 rings, 7-cm radius of curvature, (b) 14 rings, 10-cm radius of curvature, (c) 14 rings, 13-cm radius of curvature, and (d) 20 rings, 13-cm radius of curvature. For the necroses nearest the transducer, the outer rings were turned off as specified in Fig. 7.

should decrease the diameter of the transducer in order to increase the effective F number. With the concentric-ring array, this can be accomplished dynamically by reducing the acoustic power contribution of the outer rings.

Figure 6 is an example of the axial temperature profiles for a transducer with and without any outer rings turned off. Typically, the more rings turned off and the higher the resulting effective F number, the lower the secondary temperature elevations. However, increasing the F number also results in longer primary focal peaks in the axial direction, and thus the minimum number of rings should be turned off that is necessary to reduce the secondary temperature elevation to below 43°C .

Figure 7 illustrates the maximum theoretical focal ranges attainable for three transducers with different F numbers, each with 14 rings. The secondary temperature elevation at the inner focal limit for each transducer were attained by turning off the minimal number of outer rings necessary to reduce the secondary temperature elevation to below 43°C .

Simulations show that the width of the dead space between the elements affects the focal range of the transducer: the larger the dead space, the more limited the post-focal range. Available machining methods result in a dead space of approximately 0.3 mm, and as the goal of this study is practical transducer design, this minimum dead space limitation must be taken into account. Figure 8 consists of two-dimensional necrosed tissue volume boundary plots for a set of selected focal locations over the range of focus of four 14-ring transducers with F numbers 0.7, 1.0, and 1.3 and one 20-ring transducer with F number 1.3. All four of these transducers were modeled with a 0.3-mm dead space. (Note that the focus can be placed at any location within the transducer's effective range by selecting proper phasing.) In Fig. 8(a)–(c), the outer rings were turned off as specified in Fig. 7. If it were possible to construct rings that were only 2 mm wide, construction of a 20-ring transducer would then be

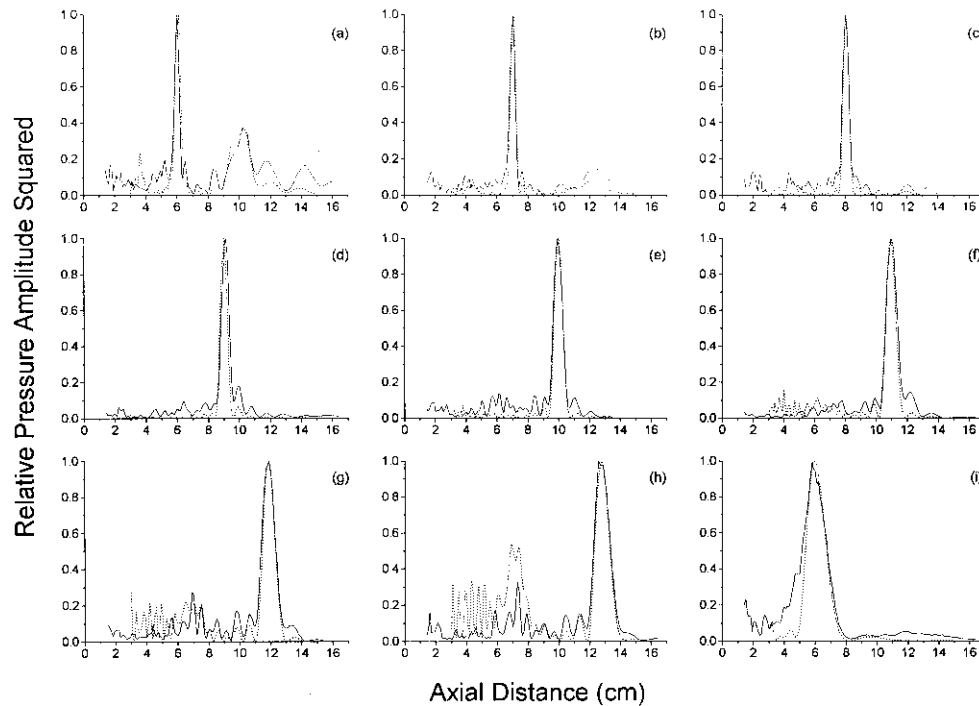


FIG. 9. Comparison of simulated transducer performance (dotted line) versus measured performance of constructed transducer (solid line). The graphs in this figure represent the axial pressure-squared distribution. The peak heights of each curve has been normalized to 1.0. Graphs (a)–(h) correspond to foci at 6, 7, 8, 9, 10, 11, 12, and 13 cm, respectively. Graph (i) illustrates the effect of turning off the outer rings by showing the theoretical and actual axial distributions for a focus at 6 cm with eight of the outer rings turned off.

possible. Figure 8(d) consists of the two-dimensional necrosed tissue volume boundary plots for a 20-ring, 13-cm radius of curvature transducer with the same 0.3-mm dead space. [In Fig. 8(d), the method of turning off the outer rings was used to reduce the secondary temperature elevations resulting when the focus is near to the surface of the transducer.]

B. Acoustic field measurements

In order to compare the fields produced by the experimental array to the simulated fields, simulations were run using the actual geometry of the constructed array sonicating into water. The phases used in these simulations were

rounded to the nearest 22.5° , the resolution at which the experimental array was driven. Figure 9 is a comparison between the pressure-squared distributions along the central axis of the experimental array and the simulation results. The theoretical predictions and the measured values of the locations of the focal peaks and their associated widths measured at full-width half-maximum along with the maximum secondary intensity are compared in Table III. The values of primary peak location and width were obtained by fitting a Gaussian function to the theoretical and measured focal peaks, and the maximum secondary intensity was defined as the maximum intensity outside of the primary focal peak

TABLE III. Comparison of the theoretical and measured performance of the constructed 14-ring, F number 1.0 transducer. The primary peak location and full-width half-maximum values were determined by fitting a Gaussian curve to the theoretical and measured data. The secondary peak intensity was determined by measuring the maximum intensity outside of the primary focal peak.

Focus(cm)	Primary focal peak				Secondary peak	
	Location (cm)		Full-width half-max (cm)		Maximum intensity (normalized)	
	Predicted	Measured	Predicted	Measured	Predicted	Measured
6	6.05	5.97	0.34	0.27	0.37	0.40
7	7.05	6.99	0.31	0.35	0.08	0.15
8	8.04	8.01	0.35	0.39	0.04	0.13
9	8.99	9.08	0.43	0.48	0.02	0.10
10	9.98	9.94	0.52	0.57	0.07	0.14
11	10.93	10.99	0.61	0.67	0.16	0.10
12	11.89	11.85	0.72	0.80	0.27	0.27
13	12.84	12.80	0.84	0.95	0.54	0.33
6 (8 rings off)	6.06	5.90	1.10	1.60	0.10	0.24

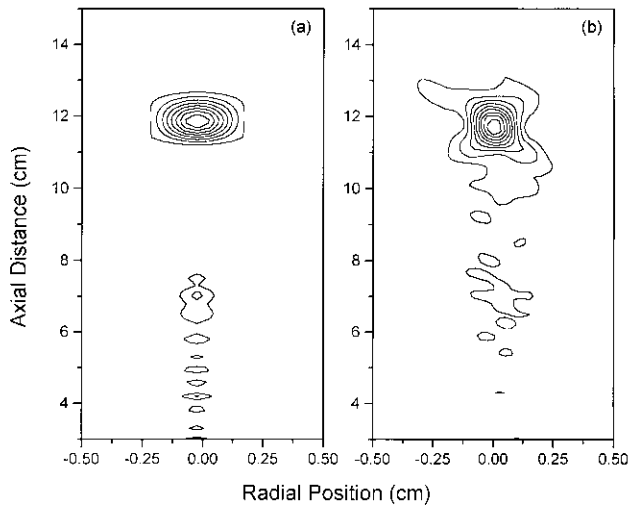


FIG. 10. Contour plots representing the two-dimensional fields of the simulated and actual transducers. (a) Theoretical field plot for a focus at 12 cm, and (b) plot of measured field from constructed array. The contour interval is 10%.

region. Figure 10 is a comparison of the actual and simulated two-dimensional contour plots for a focus of 12 cm from the base of the transducer.

The theoretical predictions for the 14-ring, F number 1.0 array were verified by the constructed array. As was shown in Table III, the difference in location of the focal peaks as predicted and measured was always less than 1 mm, except for the case when eight of the outer rings were turned off and the focus was at 6 cm. The full-width half-maximum values varied from theoretical to measured by no more than 1.1 mm, except in the latter case where the deviation was 5.0 mm. The discrepancy found in the case when the outer rings are turned off can be attributed to a lack of sufficient power control in the driving equipment that resulted in too much power being delivered to the central elements and not enough power delivered to the outer elements. The average percentage difference in secondary peak intensities between the theoretical and the predicted values was 8.3%. Thus, these data are in excellent agreement with the theoretical predictions and thus verifies the validity of the simulation results.

C. Acoustic power measurements

The simulation results show that for the manufactured transducer's geometry the maximum power per unit area occurs when the transducer is focusing at 6 cm with 8 of the outer rings turned off. For this sonication, the simulations predict a total acoustic output power of 31.4 W, or an intensity of 2.2 W/cm^2 over the inner 6 rings, in order to reach 100°C in 10 s. Each ring of the transducer was independently powered at an amplitude inversely proportional to the square root of the ring's area, such that the acoustic intensity was three times 2.2 W/cm^2 , or 6.6 W/cm^2 for each ring, where the factor of three has been added to insure adequate equipment reserve. Each ring was tested individually with the absorbing brush located approximately 2 cm from the surface of the transducer, thus insuring that cavitation was

not a problem. A summation of the output powers of all the rings results in 585 W of acoustical power. No problems were encountered with powering the rings at these desired intensities.

III. DISCUSSION

This study has illustrated the effects of number of rings, ring configuration, and F number on the focal range of the concentric-ring array. The results have shown that it is possible to construct a concentric-ring transducer of practical dimensions which allows significant focal range in the axial direction. An experimental array has been constructed and acoustic field measurements have verified the simulation results. The analysis presented here shows that the concentric-ring design promises significant advances in MRI guided ultrasound surgery.

The simulation results indicate that the focal range of a concentric-ring array is dependent on the method of ring division, yet less so than on the number of rings, radius of curvature, and overall diameter of the transducer. Dividing the transducer by the quarter-wavelength method results in an array that is capable of focusing in the range between the point chosen for the division and a point beyond the geometric focus of the transducer without producing secondary temperatures of over 43°C . When the focal point is moved beyond this range, however, the output of the transducer deteriorates at a rate greater than that of the arrays created by using the other two methods. As an example, the secondary temperature elevation for the F number 1.0 transducer focusing at 12 cm as shown in Fig. 3 is 49.3°C for the quarter-wavelength deviation method and only 42.9°C for the other two methods, resulting in almost 1 cm less focal range for the quarter-wavelength deviation method transducer.

There are certain advantages that an array with equal area rings has over an array with equal radial increments. As it is desirable to power the concentric ring array with uniform intensity, equal surface area rings would be of nearly equal impedance and would thus place similar loads on the driving amplifiers. However, as is shown in Fig. 3, the equal area transducer does not have as large a focal range as the transducers with equal radial increment or equal arc width. In addition, to create equal area rings, the ring widths must become increasingly smaller as the diameter of the ring increases. The 13-cm radius of curvature transducer with 14 rings would require the outermost ring to be only 0.178 cm wide, as opposed to the 0.357-cm width resulting from the equal radial increment method. Thus, the ring widths required for an equal element area transducer are too small to be practically constructed.

Although the equal-radial increment method was judged to yield the best configuration, the quarter-wavelength deviation method still provides useful information. Note that the innermost ring resulting from the quarter-wavelength deviation as shown in Table II is considerably larger than the corresponding ring resulting from the equal-radial increment method. Thus, a number of the inner rings on the equal-radial increment transducer could be combined without reducing the performance of the transducer as long as the total width of the combined rings remains less than that deter-

mined by the quarter-wavelength deviation criterion. Note, however, that the Table II values were generated by choosing a focal point of 5.3 cm for a 6-cm radius of curvature transducer in order to result in a total of 14 rings. To apply the quarter-wavelength deviation method in order to decrease the total number of rings by increasing the size of the center element, a focal point for the division must be chosen to produce a transducer with the desired focal range as opposed to a specific number of rings. This method suggests that for the 13- and 10-cm radius of curvature transducers, the inner two elements can be combined without degrading transducer performance.

As was shown in Fig. 5, larger F numbers result in greater focal ranges. This result suggests that the focal range of a transducer may be increased by turning off the outer rings and thus increasing the F number of the transducer. The results obtained by turning off rings, as shown in Figs. 6 and 7, can be understood by examining the geometry of the concentric-ring transducer and its effect on the phase coherence of the wavelets generated by each ring. Because the rings have a finite width, the only point along the central axis which is equidistant to all points on the surface of any given ring is the geometric focus of the transducer. However, as the focus is moved from the geometric focus, the relative phase angle between all of the points on one ring and all of the points on another ring changes by specific, discrete amounts. The finite width of the rings has the effect that the acoustic wavelets from a single ring arriving at any point along the central axis other than the geometric focus will not all be in phase. The result is ring self-cancellation and power deposition at a point other than the intended focus. The amount by which this variation of wavelet phase occurs is dependent on the width of the ring in question and on the angle between the vector normal to the surface of the ring and the line from the middle of the ring to the point of interest on the y -axis. The geometry dictates that this angle increases more rapidly for the outer elements than for the inner elements as the intended focus is moved away from the geometric focus. As either the width of the ring or this angle becomes great enough, the ring will deposit less power near the focus than elsewhere in the field. When this happens, the percentage of total power contributed by this ring must be reduced to prevent secondary foci. Turning the ring completely off allows one to extend the focal range towards the transducer without increasing the number of rings or adding other complexities to the system. This method does not apply to increasing the maximum depth of focus, because in the attempt to move the focus as deep as possible, the effective F number has been maximized. Thus, turning off the outer rings and thereby increasing the effective F number no longer has a positive contribution on the focal range.

For MRI guided ultrasound surgery, where a 10-cm focal range is desired, these results suggest that a transducer with F number 1.3 should be used to cover 9 cm of the range, from 6 to 15 cm as shown in Fig. 7. Unfortunately, if the smallest attainable ring width is 0.3 cm, approximately 14 rings is the maximum number of realizable rings when dead space between rings is taken into account. With only 14 rings, this transducer is not capable of focusing in the range

from 4 to 6 cm. Thus, another transducer specifically designed for this range of focus is necessary. The transducer with 14 rings and F number 0.7 is effective over the focal range of 4 to 8 cm, and the 2-cm overlap of focal ranges between these two transducers would allow treatment of a tumor volume located anywhere from a depth of 4 to 15 cm.

The limitations on ring width and shape are based almost entirely on the construction methods currently available. It may be possible that minimum practical ring width could be as small as to 2.0 mm, which would allow construction of a 20-ring array. In fact, as shown in Fig. 8(d), the simulations predict that a 20-ring array constructed in the same manner as the 14-ring array may cover the entire focal range from 4 to 15 cm desired for MRI guided ultrasound surgery.

IV. CONCLUSION

The large axial focal range of the concentric-ring phased array may be used to greatly reduce the volume occupied by the mechanical positioning device used in MRI guided ultrasound surgery. The results presented here have illustrated the effects of a few of the various parameters in concentric-ring transducer design. Undoubtedly, there are many other important factors governing transducer design than those discussed above, however this work should provide a good starting point for concentric-ring applicator design.

ACKNOWLEDGMENTS

This work was supported by NCI Grant No. CA46627 and a grant from General Electric Medical Systems.

- Arditi, M., Foster, S., and Hunt, W. J. (1981). "Transient fields of concave annular arrays," *Ultrason. Imag.* **3**, 37–61.
- Bihrlé, R., Foster, R. S., Sanghvi, N. T., Fry, F. J., and Donohue, J. P. (1994). "High-intensity focused ultrasound in the treatment of prostatic tissue," *Suppl. to Urology* **43**, 21–26.
- Billard, B. E., Hynynen, K., and Roemer, R. B. (1990). "Effects of physical parameters on high temperature ultrasound hyperthermia," *Ultrasound Med. Biol.* **16**, 409–420.
- Buchanan, M. T., and Hynynen, K. (1994). "Design and experimental evaluation of an intracavitary ultrasound phased array system for hyperthermia," *IEEE Trans. Biomed. Eng.* **41**, 1178–1187.
- Cain, C. A., and Umemura, S. (1986). "Concentric-ring and sector-vortex phased-array applicators for ultrasound hyperthermia," *IEEE Trans. Microwave Theory Technol.* **34**, 542–551.
- Chapelon, J. Y., Faure, P., Plantier, M., Cathignol, D., Souchon, R., Gorry, F., and Gelet, A. (1993). "The feasibility of tissue ablation using high intensity electronically focused ultrasound," *Ultrasonics Symp. Vol. 93CH3301-9*, 1211–1214.
- Cline, H. E., Schenck, J. F., Hynynen, K., Watkins, R. D., Souza, S. P., and Jolesz, F. A. (1992). "Magnetic resonance guided focused ultrasound surgery," *Comput. Assist. Tomogr.* **16**, 956–965.
- Cline, H. E., Hynynen, K., Watkins, R. D., Adams, W. J., Schenck, J. F., Ettlinger, R. H., Freund, W. R., Vetro, J. P., and Jolesz, F. A. (1995). "Focused US system for MR imaging-guided tumor ablation," *Radiology* **194**, 731–737.
- Coleman, D. J., Lizzi, F. L., Driller, J., Rosada, A. L., Chang, S., Iwamoto, T., and Rosenthal, D. (1985). "Therapeutic ultrasound in the treatment of glaucoma," *Ophthalmology* **92**, 339–346.
- Damianou, C., and Hynynen, K. (1993). "Focal heating and nearfield heating during pulsed high temperature ultrasound therapy," *Ultrasound Med. Biol.* **19**, 777–787.
- Damianou, C., and Hynynen, K. (1994). "The effect of various physical parameters on the size and shape of necrosed tissue volume during ultrasound surgery," *J. Acoust. Soc. Am.* **95**, 1641–1649.

- Darkazanli, A., Hynynen, K., Unger, E., and Schenck, J. F. (1993). "Online MRI monitoring of ultrasound surgery," *J. Magn. Reson. Imag.* **3**, 509–514.
- De Poorter, J., De Wagter, C., De Deene, Y., Thomsen, C., Ståhlberg, F., and Achten, E. (1995). "Noninvasive MRI thermometry with the proton resonance frequency (PRF) method: *in vivo* results in human muscle," *Magn. Reson. Med.* **33**, 74–81.
- Do-Huu, J. P., and Hartemann, P. (1981). "Annular array transducer for deep acoustic hyperthermia," *IEEE Ultrasonics Symp. Proc.* CH 1689-9, 705–710.
- Do-Huu, J. P., and Hartemann, P. (1982). "Deep and local heating induced by an ultrasound phased array transducer," *IEEE Ultrasonics Symp.*, 735–738.
- Fan, X., and Hynynen, K. (1992). "The effect of wave reflection and refraction at soft tissue interfaces during ultrasound hyperthermia treatments," *J. Acoust. Soc. Am.* **91**, 1727–1736.
- Fan, X., and Hynynen, K. (1994). "The effects of curved tissue layers on the power deposition patterns of therapeutic ultrasound beams," *Med. Phys.* **21**, 25–34.
- Fan, X., and Hynynen, K. (1996). "Ultrasound surgery using multiple sonications—Treatment time considerations," *Ultrasound Med. Biol.* **22**(4), 471–482.
- Fry, W. J., Barnard, J. W., Fry, F. J., Krumins, R. F., and Brennen, J. F. (1955). "Ultrasonic lesions in the mammalian central nervous system," *Science* **122**, 517–518.
- Fry, F. J., and Johnson, L. K. (1978). "Tumor irradiation with intense ultrasound," *Ultrasound Med. Biol.* **4**, 337–341.
- Heimburger, R. F. (1985). "Ultrasound augmentation of central nervous system tumor therapy," *Indiana Medicine* **78**, 469–476.
- Hynynen, K. (1991). "The threshold for thermally significant cavitation in dog's thigh muscle *in vivo*," *Ultrasound in Med. Biol.* **17**, 157–169.
- Hynynen, K., Darkazanli, A., and Unger, E., and Schenck, J. F. (1993). "MRI-guided noninvasive ultrasound surgery," *Med. Phys.* **20**, 107–115.
- Hynynen, K., Freund, W., Cline, H. E., Chung, A., Watkins, R., Vetro, J., and Jolesz, F. A. (1996). "A clinical noninvasive MRI monitored ultrasound surgery method," *RadioGraphics* (accepted for publication).
- Ibbini, M. S., and Cain, C. A. (1990). "The concentric-ring array for ultrasound hyperthermia: combined mechanical and electrical scanning," *Int. J. Hyperthermia* **6**, 401–419.
- Kishi, M., Mishima, T., Itakura, T., Tsuda, K., and Oka, M. (1975). "Experimental studies of effects of intense ultrasound in implantable murine glioma," *Proc. 2nd. European Congress on Ultrasonics in Medicine* (Amsterdam, Excerpta Medica), 28–33.
- Lele, P. P. (1962). "A simple method for production of trackless focal lesions with focused ultrasound: physical factors," *J. Physiol.* **160**, 494–512.
- Lynn, J. G., Zwemer, R. L., Chich, A. J., and Miller, A. E. (1942). "A new method for the generation and use of focused ultrasound in experimental biology," *J. Gen. Physiol.* **26**, 179–193.
- Martin, C. J., and Law, A. N. R. (1983). "Design of thermistor probes for measurement of ultrasound intensity distributions," *Ultrasonics* **21**, 85–90.
- Ocheltree, K. B., and Frizzell, L. A., (1989). "Sound field calculation for rectangular sources," *IEEE Trans. Ultrason. Ferroelectr. Freq. Control* **36**, 242–248.
- O'Neil, H. T. (1949). "Theory of focusing radiators," *J. Acoust. Soc. Am.* **21**, 516–526.
- Parker, D. L. (1984). "Applications of NMR imaging in hyperthermia: an evaluation of the potential for localized tissue heating and noninvasive temperature monitoring," *IEEE Trans. Biomed. Eng.* **31**, 161–167.
- Pennes, H. H. (1948). "Analysis of tissue and arterial blood temperatures in the resting human forearm," *J. Appl. Phys.* **1**, 93–122.
- Sapareto, S. A., and Dewey, W. C. (1984). "Thermal dose determination in cancer therapy," *Int. J. Radiat. Oncol. Biol. Phys.* **10**, 787–800.
- Skolink, M. I. (1980). *Introduction to Radar Systems* (McGraw-Hill, New York).
- Steinberg, B. D. (1976). *Principles of Aperture and Array System Design* (Wiley, New York).
- Stewart, H. F. (1982). "Ultrasonic measurement techniques and equipment output levels," in *Essentials of Medical Ultrasound*, edited by M. H. Repacholi and D. A. Benwell (Humana, Clifton, NJ), pp. 77–116.
- Vallencian, G., Harouni, M., Veillon, B., Mombet, A., Prapotnich, D., Bisset, J. M., and Bougaran, J. (1992). "Focused extracorporeal pyrotherapy: feasibility study in man," *J. Endourol.* **6**, 173–181.
- Zanelli, C. I., Hennige, C. W., and Sanghvi, N. T. (1994). "Design and characterization of a 10 cm annular array transducer for high intensity focused ultrasound (HIFU) applications," *IEEE Trans. Ultrason. Ferroelectr. Freq. Control*, 1887–1890.